Analytical and Numerical Methods in Mechanical Design
Vol.1, Issue 2, Summer & Autumn 2022, 39-57

Investigation of Failure Mechanism in Earth Dam upon Triggered Liquefaction

Farzad Peyman[1]*

[1*] *Faculty of Civil Engineering, Islamic Azad University, Qazvin Branch, Qazvin, Iran*
Received: 05 September 2022- Accepted: 07 December 2022
*Corresponding author: *f.peyman@srbiau.ac.ir*

Abstract

The behavior of the earth-dam body as a soil structure made of cohesive soil in the core and non-cohesive soil as the core supports, including water interaction upstream through earthquake upon multi-line constitutive equations, is the aim of this paper. A multi-plane mechanism-based approach is successfully employed for assigning post-liquefaction displacement of earth-dam structures. This approach is derived from total stress procedures with two major advantages:1) the triggering and post-liquefaction responses have been multi-lined into one analysis.2) the modeling of post-liquefaction element behavior is greatly improved.To sum up, a multi-plane-based framework is employed. The strength effects on integrated sampling planes and the resultant of this simulated multi-lined behavior are implemented for each finite element gauss point. This multi-plane-based model can also predict the effects of induced and inherent anisotropy plus the rotation of principal stress/strain axes through the plastic behavior of both cohesive and non-cohesive soils.The approach is presented through the simulation of the case history as the response of the lower San Fernando dam to the 1971 San Fernando earthquake. The magnitude and pattern of the predicted displacements are shown to be in good agreement with the measured values.

***Keywords*:** Liquefaction; Multi-plane; Elastic-plastic; Earth-Dam

1. Introduction

During the last decade, constitutive modeling of porous media such as soils has been the subject of numerous investigations, primarily because of the increasing awareness of the complexity of the loading conditions to which soil structures are subjected and the corresponding need for more accurate analysis for prediction of the safety of such structures. The parallel development of more powerful and efficient numerical analysis methods has motivated and allowed the use of sophisticated constitutive models beyond the linear or simple non-linear elastic-plastic constitutive laws utilized in the early stages [1-24].

Most of the models proposed are based on the theory of elastic-plasticity, incorporating different yield criteria and flow and hardening rules. Strain hardening models have been proposed according to various isotropic, kinematic, or mixed hardening rules. These models usually deal with a single or direction of principal axes of either stress or strain, or both have been observed in many tests. A model based on the invariant of stress/strain tensors, therefore, can not cope with the real behavior of soil under a complex loading program.

The task of representing the overall stress tensor in terms of micro-level stresses and the condition, number, and magnitude of contact forces has long been the aim of numerous researchers [25-28]. A multilaminate model for granular material was developed by Sadrnejad (1989) [29-30].

For a granular material such as soil that supports the overall applied loads through contact friction and cohesion, the overall mechanical response ideally may be described based on the micro-mechanical behavior of grains interconnections. Naturally, this requires the description of the overall stress, characterization of cohesivity and fabric, representation of kinematics, development of local rate constitutive relations, and evaluation of the overall differential constitutive relations in the local quantities.

Predicting soil behavior under cyclic loading is a major problem in geomechanics. The stress-strain relation of soil under cyclic loading depends on many objects; therefore, this task without mathematical models is impossible. An integrated planes-based model capable of predicting the behavior of both cohesive and non-cohesive soils based on

sliding mechanisms and the elastic behavior of particles has been presented. The capability of the model to predict the behavior of soil under arbitrary stress paths has been examined [29-31]. The rotation of principal stress axes and induced anisotropy are included rationally without any additional hypotheses. The volumetric strain in drained tests, as a state quantity in strains that should possess an essence of stress path independence by definition, is a unique quantity determined when the origin and the destination of stress paths are given.

2. Basic assumptions and discussions

Multilaminate framework, by defining the small continuum structural units as an assemblage of particles and voids that fill infinite spaces between the sampling planes, has appropriately justified the contribution of interconnection forces to overall macro-mechanics. Plastic deformations are assumed to occur due to sliding and separation/closing of the boundaries, and elastic deformations are the overall responses of structural unit bodies. Therefore, the overall deformation of any small part of the medium is composed of total elastic response and an appropriate summation of sliding, separation/closing phenomenon under the current effective normal and shear stresses on sampling planes.

3.The constitutive equations

The classical decomposition of strain increments under the concept of elastoplastic in elastic and plastic parts are schematically written as follows:

$$d\varepsilon = d\varepsilon^{e} + d\varepsilon^{p} \tag{1}$$

The increment of elastic strain ($d\varepsilon^{e}$) is related to the increments of effective stress ($d\sigma$) by:

$$d\varepsilon^{e} = [\,D^{e}\,]^{-1} \cdot d\sigma \tag{2}$$

Where $[D^{e}]^{-1}$ is the elastic compliance matrix, usually assumed as linear, and is obtained as follows:

$$D^{e}_{ijkl} = (K - \frac{2}{3}G)\cdot\delta_{ij}\cdot\delta_{kl} + G\cdot(\delta_{ik}\cdot\delta_{jl} + \delta_{il}\cdot\delta_{jk}) \tag{3}$$

Where K and G are bulk and the shear modulus, respectively.

For the soil mass, the overall stress-strain increments relation, to obtain plastic strain increments ($d\varepsilon^{p}$), is expressed as:

$$d\varepsilon^{p} = C^{p}\cdot d\sigma \tag{4}$$

Where C^{p} is the plastic compliance matrix, all effects of plastic behavior are expected to be included in C^{p}. To find out C^{p}, the constitutive equations for a typical slip plane must be considered in calculations. Consequently, the appropriate summation of all provided compliance matrices corresponding to considered slip planes yields overall C^{p}; therefore, strain increment at each stress increment is calculated as follows:

$$d\varepsilon^{p} = \frac{1}{n}\sum_{i=1}^{n} w_i \cdot [\,L_{\varepsilon}\,]^{T}\cdot C_i^{p}\cdot[\,L_{\sigma}\,]\cdot d\sigma' \tag{5}$$

L_{ε} and L_{σ} are transformation matrices for strain and stresses, respectively, and n is the number of planes.

4. Constitutive equations for a sampling plane

A *sampling plane* is defined as a boundary surface which is a contacting surface between two structural units of polyhedral blocks. These structural units are parts of a heterogeneous continuum, and for simplicity, they are defined as a completely homogeneous and isotropic material. Therefore, all heterogeneity's behavior is supposed to appear in the inelastic behavior of corresponding slip planes. Figure 1 shows these defined planes (say 13). This number may be chosen as any number; however, based on some numerical experiences, 13 is found to fit a rationally justified and possess enough power to show any distribution through the material. The direction cosines and weighted coefficients

carried out and employed using the numerical integration of the rule for calculation of stress/strain/compliance tensor of each plane are presented in Table 1.

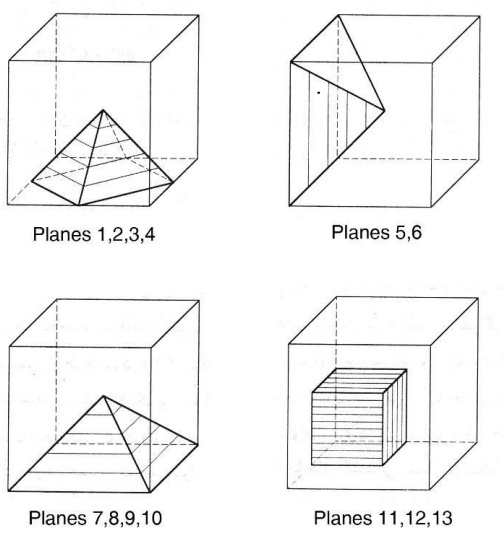

Fig. 1. Definition of 13 planes

Table 1. Cosines of the normal axis and the weight coefficients for numerical integration

Plane No	Normal Axis			w_i
	l_i	m_i	n_i	
1	$\frac{1}{\sqrt{3}}$	$\frac{1}{\sqrt{3}}$	$\frac{1}{\sqrt{3}}$	$\frac{27}{840}$
2	$\frac{1}{\sqrt{3}}$	$-\frac{1}{\sqrt{3}}$	$\frac{1}{\sqrt{3}}$	$\frac{27}{840}$
3	$-\frac{1}{\sqrt{3}}$	$\frac{1}{\sqrt{3}}$	$\frac{1}{\sqrt{3}}$	$\frac{27}{840}$
4	$-\frac{1}{\sqrt{3}}$	$-\frac{1}{\sqrt{3}}$	$\frac{1}{\sqrt{3}}$	$\frac{27}{840}$
5	$\frac{1}{\sqrt{2}}$	$\frac{1}{\sqrt{2}}$	0	$\frac{32}{840}$
6	$-\frac{1}{\sqrt{2}}$	$\frac{1}{\sqrt{2}}$	0	$\frac{32}{840}$
7	$\frac{1}{\sqrt{2}}$	0	$\frac{1}{\sqrt{2}}$	$\frac{32}{840}$
8	$-\frac{1}{\sqrt{2}}$	0	$\frac{1}{\sqrt{2}}$	$\frac{32}{840}$
9	0	$-\frac{1}{\sqrt{2}}$	$\frac{1}{\sqrt{2}}$	$\frac{32}{840}$
10	0	$\frac{1}{\sqrt{2}}$	$\frac{1}{\sqrt{2}}$	$\frac{32}{840}$
11	1	0	0	$\frac{40}{840}$
12	0	1	0	$\frac{40}{840}$
13	0	0	1	$\frac{40}{840}$

4.1. Yield criterion

In this constitutive formulation, the yield criterion is defined by the absolute ratio of shear stress (τ_i) to the normal effective stress (σ'_{ni}) on i^{th} sampling plane. The simplest form of yield function, i.e., a straight line on t versus σ_n space, is adopted. As the ratio τ/σ_n increases, the yield surface, represented by the straight line, rotates anti-clock-wise due to hardening and approaches the Mohr-Columbus failure line. Finally, failure on the corresponding plane takes place.

The equation of yield function is formulated as follows:

$$F_i(\tau_i, \sigma_{ni}, \eta_i) = \tau_i - C_i - \eta_i \cdot \sigma_{ni} \quad (6)$$

Where η_i=tan(α_i) is a hardening parameter and is assumed as a hyperbolic function of plastic shear strain on the i^{th} plane, α_i is the slope of the yield line, and C_i is the cohesivity of soil.

An elastic domain is considered to provide elastic behavior of cohesionless material whenever the stress path direction changes. This domain, as shown in Figure 2, is small and negligible.

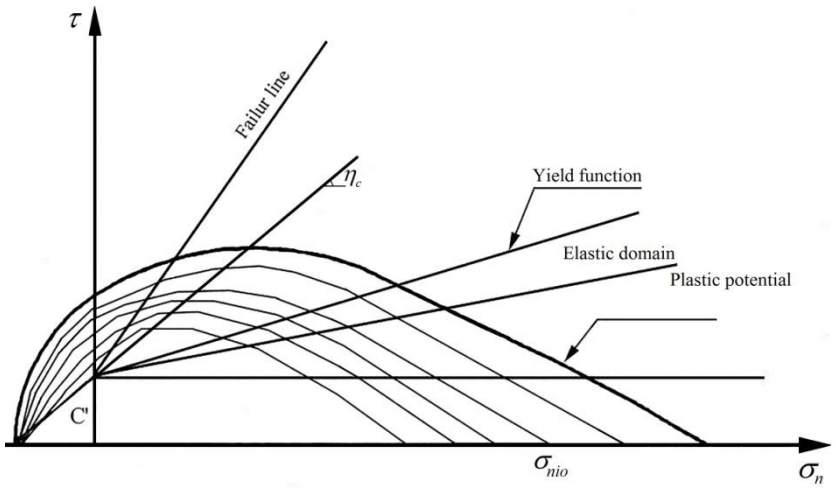

Fig. 2. Functions in τ–σ_n

Therefore, the value of ϕ_e for all soil grains is assumed to be the same. However, to consider the cohesivity of soil at the start of the stress increment, another elastic domain between the lines corresponding to τ=±C has been defined. This domain also is shown in Figure 2. Consequently, the behavior of soil for τ<C_i is supposed to be elastic.

4.2. Plastic potential function

The potential plastic function is stated in terms of τ_i and σ_i for the t versus σ_n space as follows:

$$F_i(\tau_i, \sigma_{ni}, \eta_i) = \tau_i - C'_i - \eta_i \cdot \sigma_{ni} \quad (7)$$

Where η_c is the slope of the critical state line and σ_{nic} is the value of effective normal stress in the i^{th} plane when τ_i=C'_i. Typical presentations of this function are shown in Figure 2. The gradient of this function represents contraction and dilatant behavior in the ranges:

$0.0 \le \tau_i \le \sigma_{ni}\eta_c$ (contractant behavior) (8)

$\tau_i \ge \sigma_{ni}\eta_c$ (dilatant behavior) (9)

Derivative of this function is found as:

$$\partial\psi_i / \partial\sigma_i = \{1.0, \eta_c - \eta_i\}^T \quad (10)$$

Where η_i is the hardening parameter or the slope of the yield line in i^{th} plane.

Dilatancy is positive if $\eta_i > \eta_c$ and negative if $\eta_i > \eta_c$. On the critical state line $\eta_i = \eta_c$, and there is no volumetric plastic strain for the soils predominantly composed of clay, a yield function the same as potential can be employed with the associated flow rule. In this case, a volumetric hardening rule besides shear hardening can present volumetric change during plasticity.

In the theory of plastic flow, consistency condition is necessary for a yield criterion to be satisfied as long as the material is in a plastic state. Mathematically, this condition is stated as follows:

$$\{\partial F_i/\partial \sigma_i\}^T \cdot d\sigma_i + \{\partial F_i/\partial K_i\}^T \cdot dKi = 0.0 \tag{11}$$

Where in the first loading process $K_i = \varepsilon^p{}_i$ and ε_i is plastic strain on the i^{th} plane. This relation can also be expressed in another form as:

In the first loading process, $K_i = \varepsilon^p{}_i$ and ε_i are the plastic strain on the i^{th} plane. This relation can also be expressed in another form:

$$\partial \varepsilon_i^p = \{1/H_{pi}\} \cdot \{\partial F_i/\partial \sigma_i\}^T \cdot \{\partial \psi_i/\partial \sigma_i\} \cdot d\sigma_i \tag{12}$$

Where H_{pi} is defined as the hardening modulus of i plane and is obtained as follows:

$$H_{pi} = -\{\partial F_i/\partial K_i\}^T \cdot \{\partial \psi_i/\partial K_i\} \tag{13}$$

therefore,

$$d\varepsilon_i^p = C_i^p \cdot d\sigma_i \tag{14}$$

where:

$$C_i^p = \{1/H_{pi}\} \cdot \{\partial F_i/\partial \sigma_i\}^T \cdot \{\partial \psi_i/\partial \sigma_i\} \tag{15}$$

$C^p{}_i$ is a 2×2 matrix and, as a whole, represents the plastic resistance corresponding to the i^{th} active plane in plasticity and must be summed up as the contribution of this plane with the others after transforming into a 6×6 size in global coordinate. Accordingly, the conceptual numerical integration of a multi-laminate framework presents the following summation for computing C^p.

$$C^p = 4\Pi \cdot \sum_{i=1}^{n} w_i \cdot L^T \cdot C_i^p \cdot L \tag{16}$$

Where w_i is the weight coefficient, C^p is the global plastic compliance matrix corresponding to a single point in the medium, and L is the transformation matrix for the corresponding plane. n is the employed number of planes.

4.3. Hardening rule

This model employed an isotropic plastic shear hardening rule for each plane. A simple function simulates the best variation of this property during the plastic flow, which has been represented as a hyperbolic function as follows:

$$|\eta_i| = \frac{K_i \cdot \tan(\phi_f)}{A_i + K_i} \tag{17}$$

Where, $Ki = (\varepsilon^{pt}{}_i - \varepsilon^{pt}{}_{oi})$, ϕ_f is the peak internal frictional angle, and A_i is a soil parameter. $\varepsilon^{pt}{}_i$ and $\varepsilon^{pt}{}_{oi}$ are current and initial values of plastic shear strain on the i^{th} plane. At first, loading $\varepsilon^{pt}{}_{oi}$ is equal to zero, and its value is updated at each change of load increment sign. η_i starts from ϕ_e, grows with the plastic shear strain, and slowly approaches the failure line. However, as stated, dense soils it has to rotate back towards the critical state line slowly.

4.4. First loading

The behavior of non-cohesive soil is assumed to be elastic in a small zone, as shown in Figure 2. This conforms with a small η_i value equal to tan(ϕ_e).

A simple form of variation of η_i is a hyperbolic function that has been considered. However, the range of variation of η_i is between -tan(ϕ_f) and +tan(ϕ_f). The following relation is an equation used for the first loading.

$$|\eta_i| = \frac{(\varepsilon_i^{pt} - \varepsilon_{oi}^{pt}) \cdot (m \cdot tan(\phi_f) - \eta_{oi})}{A_i + (\varepsilon_i^{pt} - \varepsilon_{oi}^{pt})} + \eta_{oi} \quad (18)$$

A_i is a material constant, and for the first loading, it is equal to A_o, where A_o is the initial value of this parameter. η_{oi} and $\varepsilon^{pt}{}_{oi}$ are the values of η_i and $\varepsilon^{pt}{}_i$ when the last change in the stress path direction has occurred. For the first loading $\varepsilon^{pt}{}_{oi}$ and η_{oi} are equal to zero. *m* for first loading is equal to +1. The value of A_o is found by trial and error by comparing computer results with experimental results of triaxial compression tests.

For cohesive soil, the same hardening functions are employed except within the domain $\tau = \pm C_i$ where the soil behavior is assumed to be elastic. Therefore, as the shear stress on any plane exceeds this value, the value of η_i can be obtained by the same equations presented.

4.5. Un-loading

The value of *A* must be changed to obtain comparable theoretical and experimental results. Another reason for this is the different shape of the hysteresis loop when cyclic loading takes place at different positions. Value *A* of obtained from numerical experiments is given by:

Equations (19) and (20) are valid for unloading, and *m* must be equal to -1 for the unloading process. The value of η_i approaches -tan(ϕ_f) while $\varepsilon^{pt}{}_i$ is large enough compared to *Ai*.

$$A_i = A_o + 0.075 \cdot \varepsilon_{oi}^{pt} \quad (19)$$

4.6. Re-loading

The variation of η_i for the reloading process is similar to unloading, although the limit value of η_i is +tan(ϕ_f).*m* is equal to +1, and the value of *A* must change. The new value of A_i is shown as follows :

Where $\varepsilon^{pt}{}_{oi}$ and η_{oi} are the values of $\varepsilon^{pt}{}_i$ and η_i at the start of the unloading process. $\varepsilon^{pt}{}_{oi}$ and η_{oi} are similar values at the start of the reloading process.

$$A_i = (\bar{\varepsilon}_{oi}^{pt} - \varepsilon_{oi}^{pt}) \cdot \{(tan(\phi_f) - \eta_{oi}) / (\bar{\eta}_{oi} - \eta_{oi}) - 1.0\} \quad (20)$$

Finally, this form of variation for η_i as a unique equation at each process can produce hysteresis energy loops with different widths. The higher the absolute values of $\varepsilon^{pt}{}_{oi}$ and η_{oi} the higher the width of hysteresis energy loops produced.

Finally, this form of variation for η_i as a unique equation at each process can produce hysteresis energy loops with different widths. The higher the absolute values of $\varepsilon^{pt}{}_{oi}$ and η_{oi}, the higher the width of hysteresis energy loops produced.

5. The model response under undrained conditions

The principle of effective stress for a saturated soil element is stated in macro scale and incremental form as follows:

$$d\sigma = d\sigma' + m \cdot dU \quad (21)$$

Where σ and σ' are representatives of total and effective stresses vectors, respectively, m is the constant operator vector equal to *{1,1,1,0,0,0}*, U is the excess pore water pressure, and d is used for representing small increments.

It can also be assumed that in a fully undrained case, the skeleton volume change is precisely equal to the change in pore water volume. Equation (22) can be rewritten as:

$$dU = K_f \{m\}^T \cdot d\varepsilon \tag{22}$$

Where K is obtained as follows [32]:

$$\frac{1}{K_f} = \frac{1}{K_w} + \frac{1-\vartheta}{K_s} \tag{23}$$

K_w is the bulk modulus of water, and ϑ is the initial porosity. Retaining the elastoplastic constitutive law, it is presented as follows:

$$d\sigma = D^{ep} \cdot d\varepsilon \tag{24}$$

$$d\sigma = D^{ept} \cdot d\varepsilon \tag{25}$$

Where D^{ep} and D^{ept} are effective and total stress-strain matrices. Therefore,

$$D^{ept} = D^{ep} + K_f \{m\}^T \cdot \{m\} \tag{26}$$

where,

$$D^{ep} = [C^{ep}]^{-1} \tag{27}$$

$$C^{ep} = C^e + C^p \tag{28}$$

C^e, C^p, and C^{ep} are compliance elasticity, plasticity, and elastoplastic matrices.

According to the incremental algorithm, C^{ep} computed in the previous step can be used for the current step; therefore, the solution will not remain indeterminate. Consequently, D^{ept} can be employed to calculate strain increments upon total stress increment tensor.

The general dynamic force equilibrium equation is written as follows:

$$\sigma_{ij} + f_i = M\delta_i + C\delta_i \tag{29}$$

Where σ_{ij} is the stress tensor, f_i is external force, M and C are mass and damping, i and j stand for coordinate axes, and δ is the displacement. Upon use of the integration rule and Green's theory, this equation can be presented as follows:

$$-\int B^T \sigma \cdot dV + M\delta + C\delta + f = 0 \tag{30}$$

where,

$$-\int N^T f_s \cdot dS - \int N^T f_b \cdot dV = f \tag{31}$$

$$\rho \int N^T N \cdot dV = M \tag{32}$$

$$c \int N^T N \cdot dV = C \tag{33}$$

Where ρ and c are density and damping, respectively. Equation (30) yields:

$$M\delta + C\delta + K\delta - QU + f = 0 \tag{34}$$

where,

$$K = \int B^T D^{ep} B \cdot dV \tag{35}$$

$$Q = \int B^T m N_U \cdot dV \tag{36}$$

Conceptually, Q is a matrix presenting equilibrium and continuity interaction.

To employ a simple numerical solution of equation (34), it can be written in a general form as follows:

$$K\delta + f = 0 \tag{37}$$

where,

$$K = \int B^T D^{ep} B \cdot dV + 3K_f \int B^T B \cdot dV \tag{38}$$

6. Accumulation of pore pressure

Usually, there are some hydrostatic pore water pressures in saturated soil. However, pore water pressure can be divided into static and excessive, and pore spaces are assumed to be saturated with water. The static water pressure is accounted for by subtracting the buoyancy force from the weight of particles.

The excessive pore water pressure is obtained by assuming water as an elastic medium without shear resistance. Under cyclic loading, a hysteresis loop of dissipated energy takes place. Consequently, while plastic strain takes place, some volumetric strain shall be obtained in the soil and water. The difference between these two strain values, multiplied by the bulk modulus of the soil and water mixture, can present a pore water pressure increment.

7. San Fernando dam

This dam, located near Los Angeles, failed by a 6.6 Richter earthquake on 9th-Feb.-1971 [33-35] the complete failure shape of this dam is shown in Figure 3-a, and the base acceleration time history of this earthquake is shown in Figure 3-b. The following parameters are obtained according to the calibration of model results with two test results on non-cohesive and cohesive samples, as shown in Figures 4-a and 4-b. For cohesive soil used in the core:

E= ٩٠٠٠KPa, ν=0.3, ϕ=2٠°, η_c=0.98tanϕ, C'= ١KPa, A=0.001, γ=15 KN/m^3.

For non-cohesive soil used in the dam body except the core:

E= ٩٦٦٧KPa, ν=0.377, ϕ=32.62°, η_c=0.75tanϕ, C'=0, A=0.001 ,γ=16.69 KN/m^3.

The dam's height is 50m, the length is 275m, and the water height at the time of the earthquake was 36m. The aim of this computation is elastoplastic behavior during 12 seconds of earthquake base acceleration time history.

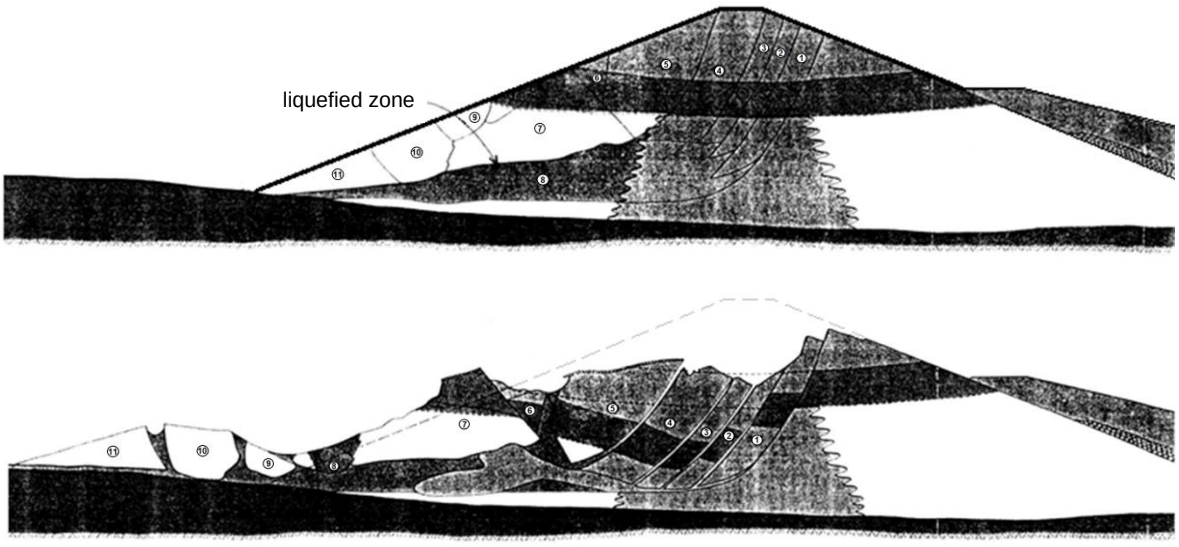

Fig. 3-a. San Fernando Dam before and after liquefaction

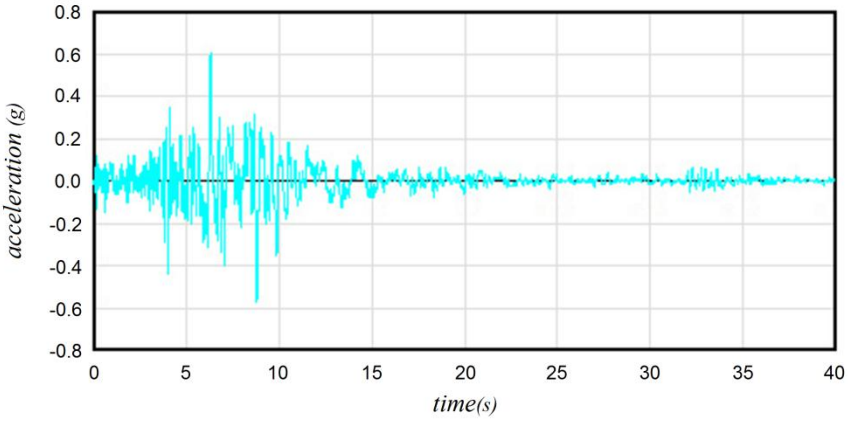

Fig. 3-b. Baseline acceleration of San Fernando earthquake input

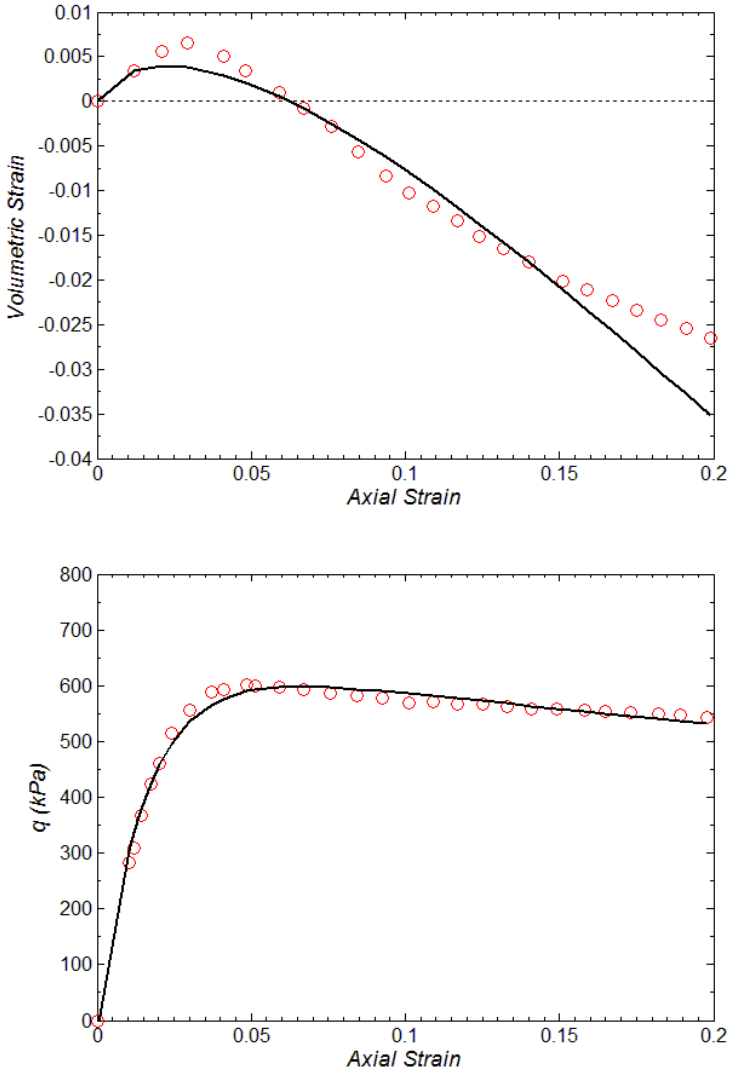

Fig. 4-a. Calibration of the test results of dam shell materials and numerical model in two spaces: ε_v:ε_1 and q:ε_1

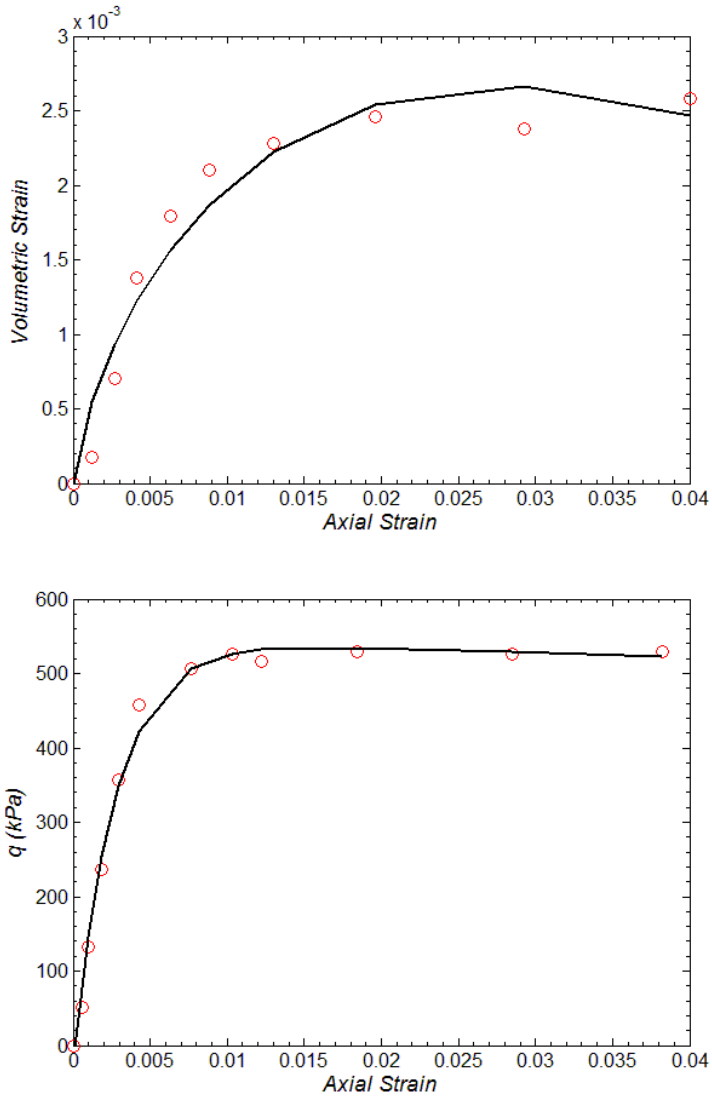

Fig. 4-b. Calibration of the test results of dam core materials and numerical model in two spaces: ε_v:ε_1 and q:ε_1

8. Numerical model

A three-dimensional mesh is developed in three vertical 5m thick layers, as shown in Figure 5-a. Figure 5-b shows the mid-layer mesh, including the core. The employed time increment is 0.02 seconds, much shorter than a quarter of the minor earthquake period. The deformed shape of the mid-layer at starting time of failure is shown in Figure 6-a. Pore water pressure and effective mean stress contours at the starting time of instability are shown in Figures 6-b and 6-c, respectively. The zone, including the highest pore water pressure and negligible effective mean stress, is the center where liquefaction was taken place [36]. Comparing these Figures with Figure 3 leads to imagine what happens at the start of instability. At this stage, the liquefied zone started to move out of the dam body, and consequently, the upper part slid down. The post-seismic motion may have sometimes forced the slid particles to settle down and deform more. This judgment agrees with the final dam failure shape shown in Figure 3. The multilaminate model and finite element developed program can identify two forms of failure based on the shear and tension of defined sampling planes. The

identified plastic shear strain value for a failed plane is %15, and for tension is %5. Figure 6-d shows the failed gauss points to introduce the global form of collapsed band.

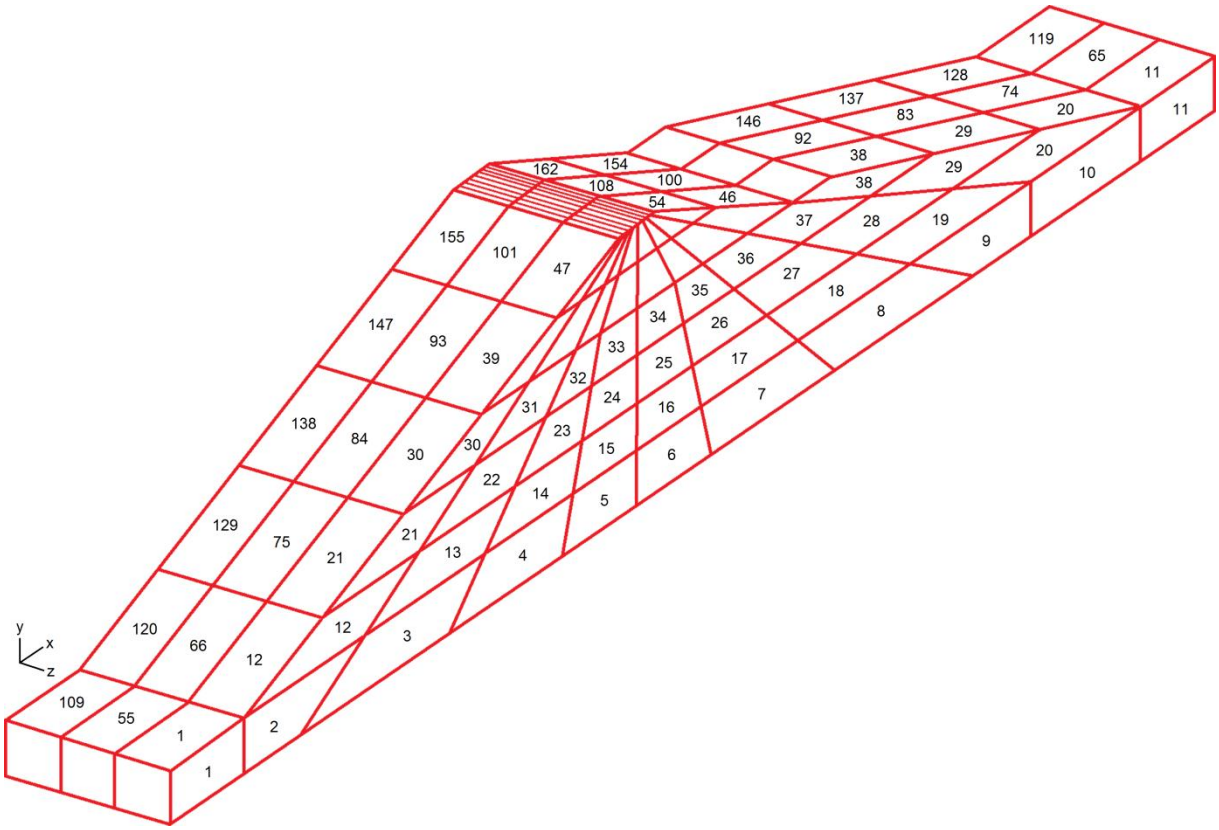

Fig. 5-a. 3D modeling of San Fernando Dam and numbering of eight-node elements

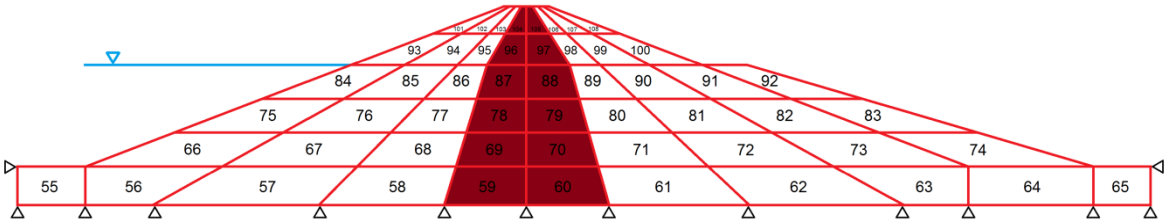

Fig. 5-b. The number of elements and characteristics of the middle layer in the modeling of the San Fernando dam

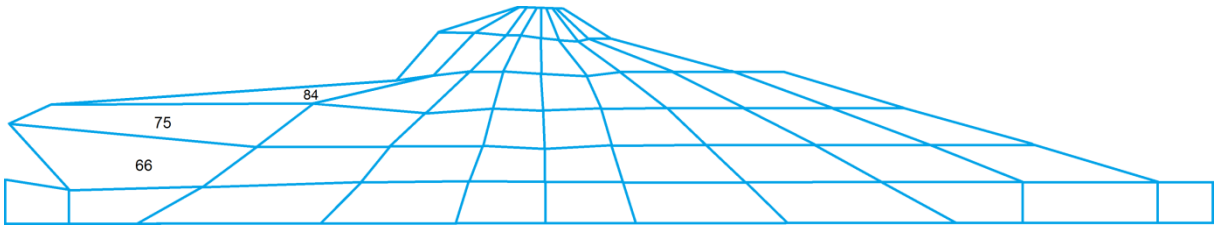

Fig. 6-a. Deformation of dam elements after an earthquake

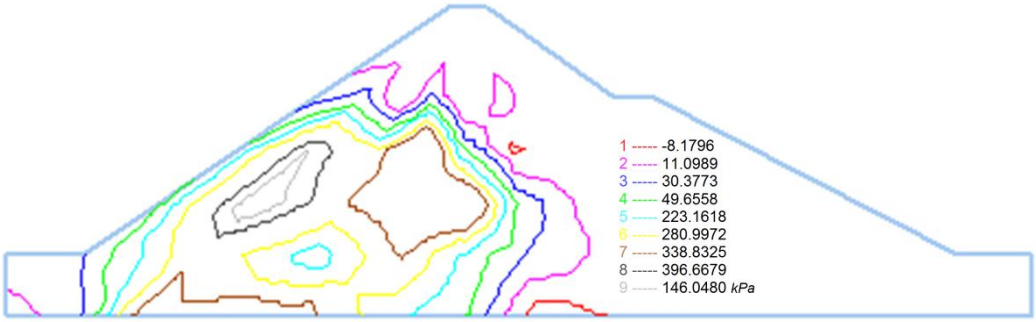

Fig. 6-b. Pore water pressure contours

Fig. 6-c. Effective stress contours

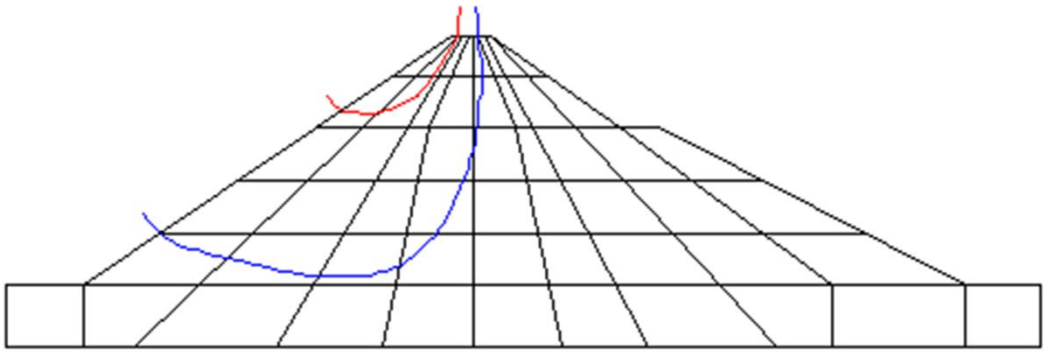

Fig. 6-d. Shear failure paths in the dam

To clarify details of the first sheared plane (plane 6, gauss point 4, element 75), the stress path, strain stress, shear stress history, and normal stress history are shown in Figures 7-a to 7-d, respectively. Through the elements represented cohesive soil in the core, plane number 2 of gauss point 8 of element number 87 tended to fail upon hydraulic fracture. The stress path, strain-stress, shear stress history, and the normal stress history of this plane are shown in Figures 8-a to 8-d, respectively. Figures 8-e to 8-g are the time histories for this plane's shear stress, normal stress, and pore water pressure. Also, to show the model's ability, Figures 9-a to 9-c show the plastic elements in the initial stages of loading, the liquefaction areas during the earthquake, and the tensile failure area in the dam core, respectively.

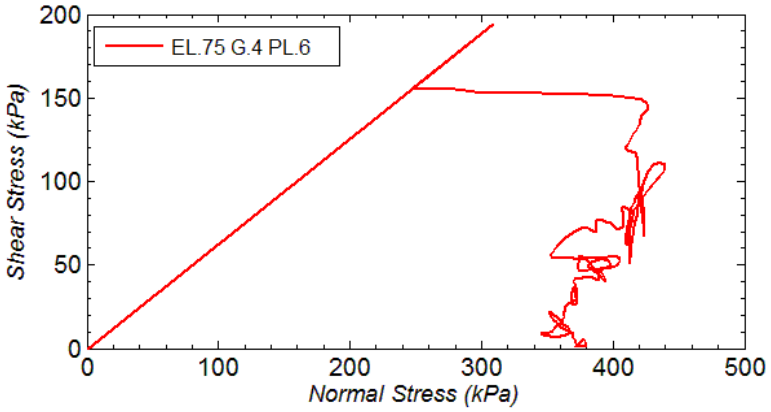

Fig. 7-a. Shear stress-Normal stress diagram in element number 75, Gauss point 4, page number 6

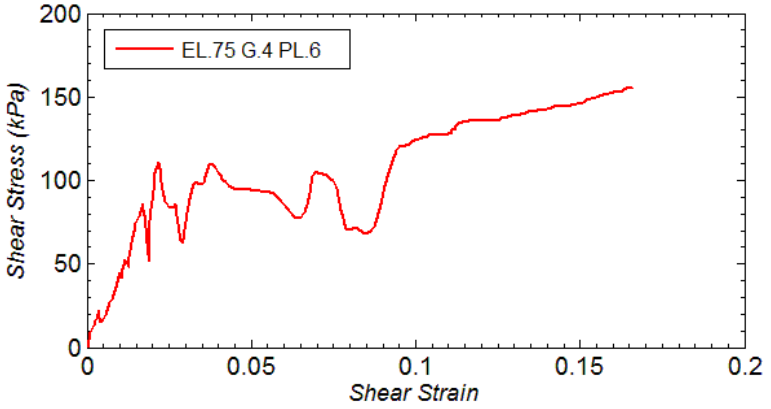

Fig. 7-b. Shear stress-Shear strain diagram in element number 75, Gauss point 4, page number 6

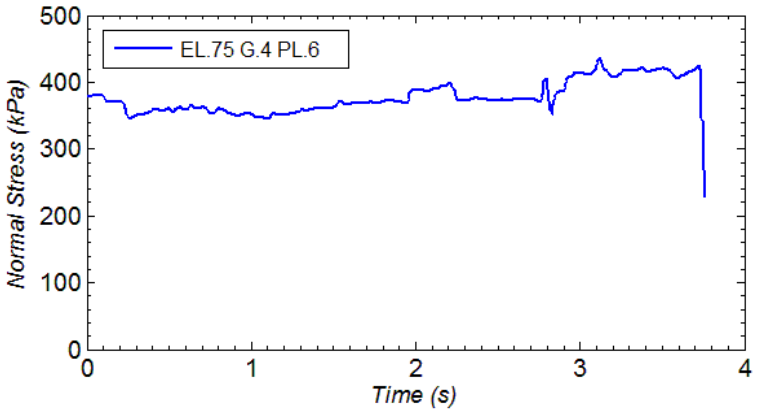

Fig. 7-c. Time history of normal stress in element number 75, Gauss point 4, page number 6

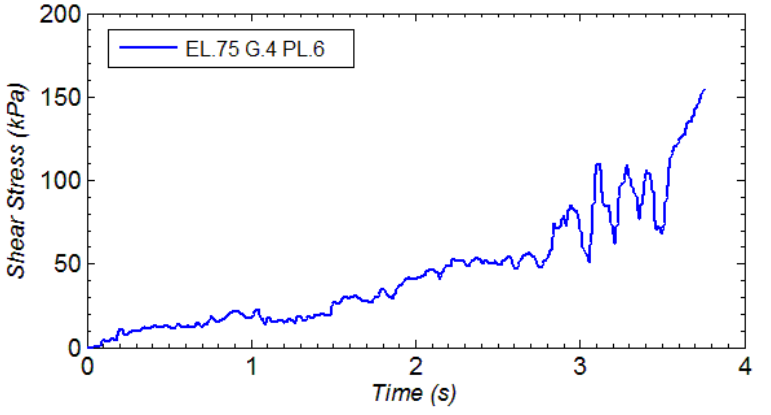

Fig. 7-d. Time history of shear stress in element number 75, Gauss point 4, page number 6

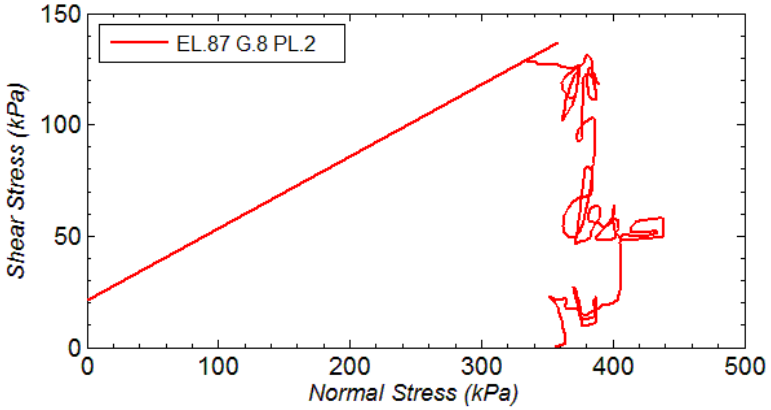

Fig. 8-a. Shear stress-Normal stress diagram in element number 87, Gauss point 8, page number 2

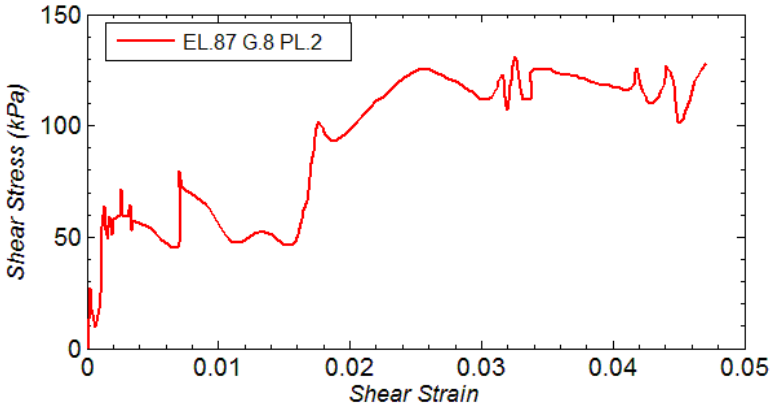

Fig. 8-b. Shear stress-Shear strain diagram in element number 87, Gauss point 8, page number 2

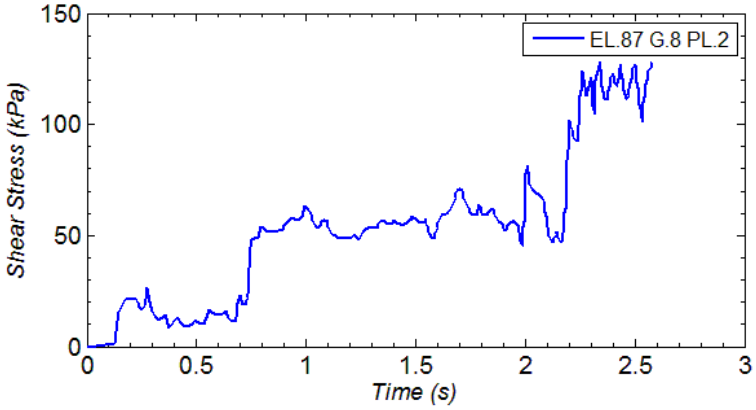

Fig. 8-c. Time history of shear stress in element number 87, Gauss point 8, page number 2

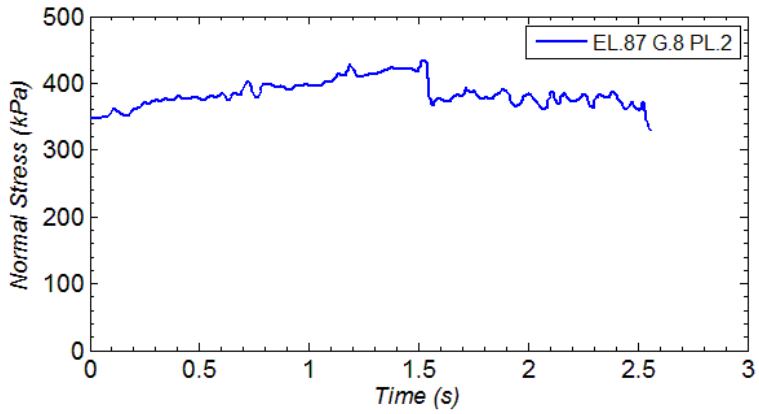

Fig. 8-d. Time history of normal stress in element number 87, Gauss point 8, page number 2

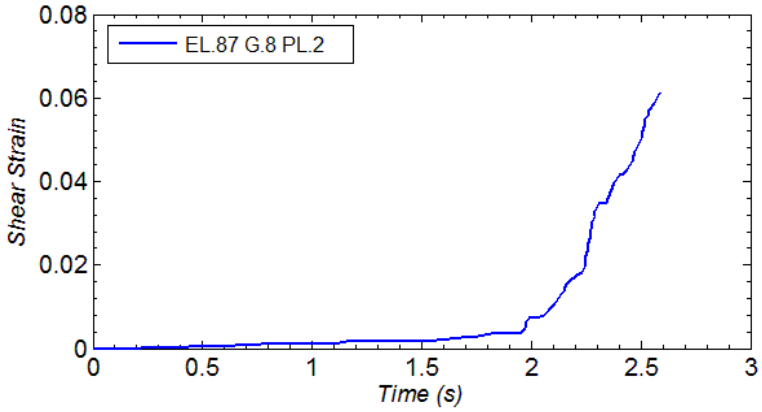

Fig. 8-e. Time history of shear strain in element number 87, Gauss point 8, page number 2

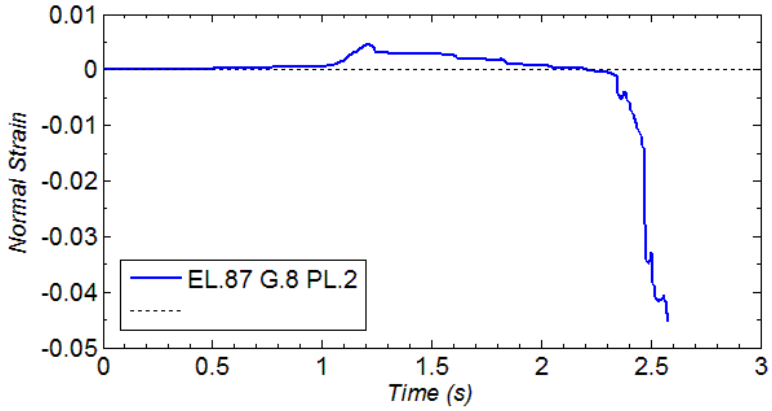

Fig. 8-f. Time history of normal strain in element number 87, Gauss point 8, page number 2

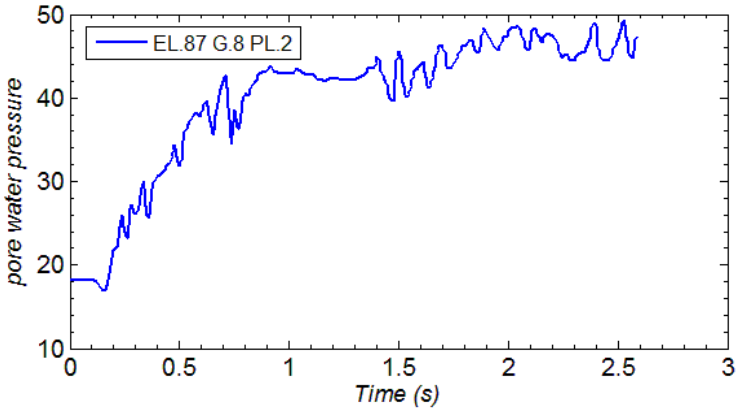

Fig. 8-g. Time history of pore water pressure in element number 87, Gauss point 8, page number 2

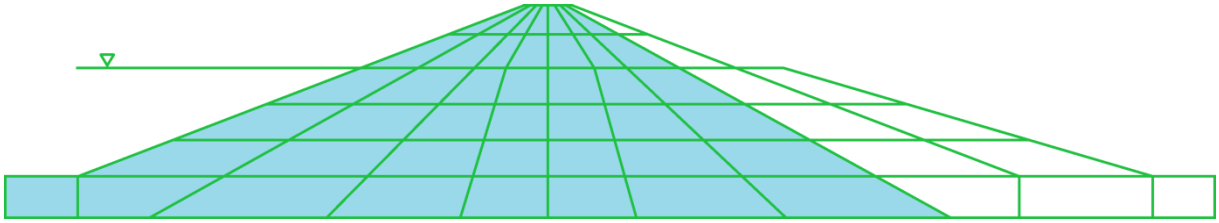

Fig. 9-a. Plastic elements in the initial stages of loading

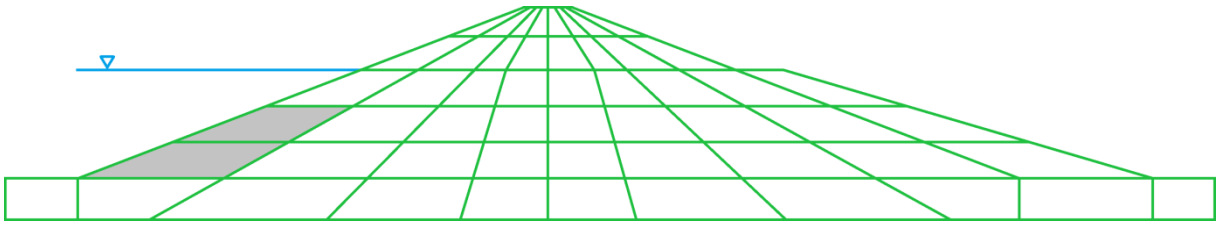

Fig. 9-b. Liquefaction areas during earthquakes

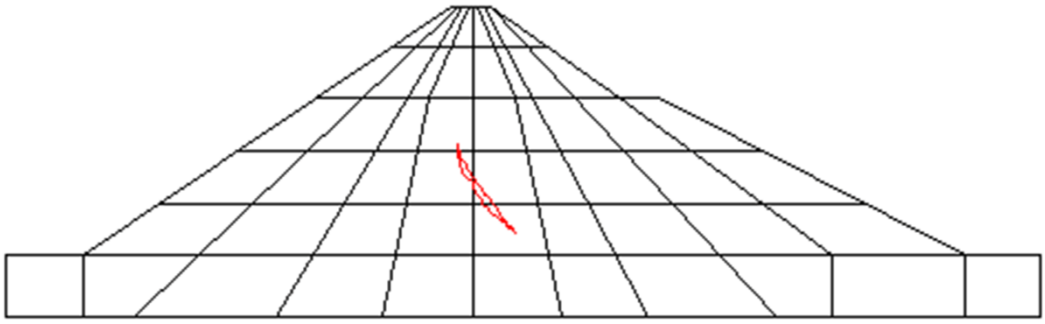

Fig. 9-c. Tensile failure zone in the core of the dam

9. Conclusions

A unique model capable of predicting the behavior of both non-cohesive and cohesive, either in saturated or dry conditions, based on sliding mechanisms, elastic behavior of particles, and a higher effective hydrostatic pressure due to liquefaction in a non-cohesive and hydraulic fracture in cohesive soil has been presented. The concept of a multi-laminate framework was applied successfully in the dynamic analysis of three-dimensional soil structures. This is

achieved using simplified, applicable, effective, and easily understandable relations between micro and macro scales. These relations demonstrate an easy way to handle any heterogeneous material property as well as the mechanical behavior of materials.

This model can solve a three-dimensional plasticity problem with a relatively simple theory based on the phenomenological description of two-dimensional plastic deformation and kinematic hardening of materials. This is achieved in such a way that the application of some difficult tasks, such as induced anisotropy and rotation of principal stress and strain axes where there is no coaxial taking place during plastic flow, are out of constitutive relations. Accordingly, the sampling plane constitutive formulations provide convenient means to classify loading events, generate history rules and formulate independent evolution rules for local variables.

The behavior of soil has also been modeled upon cyclic loading leading to liquefaction, hydraulic fracture, and failure instability based on a semi-microscopic concept very close to the reality of particle movement in soils. Therefore, the solution to any complexities involved in the change of strength due to the build-up of pore water pressure and volume change of the soil skeleton can be obtained and presented.

References

Sadrnejad, S. A. "A general multi-plane model for post-liquefaction of sand." Iranian Journal of Science and Technology 31.B2 (2007): 123.

Sadrnejad, Seyed Amirodin, and Hamid Karimpour. "Drained and undrained sand behaviour by multilaminate bounding surface model." (2011): 111-125.

Daouadji, Ali, et al. "Experimental and numerical investigation of diffuse instability in granular materials using a microstructural model under various loading paths." Géotechnique 63.5 (2013): 368-381.

Ghafghazi, M., D. A. Shuttle, and J. T. DeJong. "Particle breakage and the critical state of sand." Soils and Foundations 54.3 (2014): 451-461.

Fang, H. L., H. Zheng, and J. Zheng. "Micromechanics-based multimechanism bounding surface model for sands." International Journal of Plasticity 90 (2017): 242-266.

Loukidis, D., and R. Salgado. "Modeling sand response using two-surface plasticity." *Computers and Geotechnics* 36.1-2 (2009): 166-186.

Jin, Yinfu, et al. "Unified modeling of the monotonic and cyclic behaviors of sand and clay." Acta Mechanica Solida Sinica 28.2 (2015): 111-132.

Woo, Sang Inn, and Rodrigo Salgado. "Bounding surface modeling of sand with consideration of fabric and its evolution during monotonic shearing." International Journal of Solids and Structures 63 (2015): 277-288.

Sun, Yifei, and Yang Xiao. "Fractional order plasticity model for granular soils subjected to monotonic triaxial compression." International Journal of Solids and Structures 118 (2017): 224-234.

Heidarzadeh, Heisam, and Mohammad Oliaei. "Development of a generalized model using a new plastic modulus based on bounding surface plasticity." *Acta Geotechnica* 13.4 (2018): 925-941.

Yang, Yanxin, and Edward Kavazanjian Jr. "Numerical evaluation of liquefaction-induced lateral spreading with an advanced plasticity model for liquefiable sand." *Soil Dynamics and Earthquake Engineering* 149 (2021): 106871.

Yang, Yanxin, and Edward Kavazanjian Jr. "Numerical evaluation of liquefaction-induced lateral spreading with an advanced plasticity model for liquefiable sand." *Soil Dynamics and Earthquake Engineering* 149 (2021): 106871.

Yang, Yanxin, and Edward Kavazanjian Jr. "Numerical evaluation of liquefaction-induced lateral spreading with an advanced plasticity model for liquefiable sand." *Soil Dynamics and Earthquake Engineering* 149 (2021): 106871.

Wang, Zhiliang, and Fenggang Ma. "Bounding surface plasticity model for liquefaction of sand with various densities and initial stress conditions." *Soil Dynamics and Earthquake Engineering* 127 (2019): 105843.

Zhang, Fuguang, et al. "DEM analysis of cyclic liquefaction behaviour of cemented sand." *Computers and Geotechnics* 142 (2022): 104572.

Fang, Qin, et al. "Mesoscopic investigation of the sand particulate system subjected to intense dynamic loadings." *International Journal of Impact Engineering* 89 (2016): 62-71.

Peyman Farzad, and Seyed A. Sadrnejad. "Liquefied Residual Strength of Undrained Sand upon A Parametric Approach to Hypo-elastic Model" Numerical Methods in Civil Engineering (2017).

Sadrnejad, S. A., and Sh Shakeri. "Fabric assessment of damaged anisotropic geo-materials using the multi-laminate model." International Journal of Rock Mechanics and Mining Sciences 91 (2017): 90-103.

Sadrnejad, S. A., and Sh Shakeri. "Multi-laminate non-coaxial modelling of anisotropic sand behavior through damage formulation." Computers and Geotechnics 88 (2017): 18-31.

Zhang, Jinhua, Yadong Zhang, and Qin Fang. "Numerical simulation of shock wave propagation in dry sand based on a 3D mesoscopic model." *International Journal of Impact Engineering* 117 (2018): 102-112.

Dashti, Hadi, Seyed Amirodin Sadrnejad, and Navid Ganjian. "A novel semi-micro multilaminate elasto-plastic model for the liquefaction of sand." *Soil Dynamics and Earthquake Engineering* 124 (2019): 121-135.

Li, Haoyang, et al. "Three-dimensional mesoscopic investigation on equation of state for dry sand under shock compression." *International Journal of Impact Engineering* 160 (2022): 104060.

Evangelista Jr, Francisco, and José Fabiano Araújo Moreira. "A novel continuum damage model to simulate quasi-brittle failure in mode I and mixed-mode conditions using a continuous or a continuous-discontinuous strategy." *Theoretical and Applied Fracture Mechanics* 109 (2020): 102745.

Peyman, Farzad, and Seyed A. Sadrnejad. "Analysis of concrete crack growth based on micro-plane model." Structural Concrete 19.3 (2018): 930-945.

Zienkiewicz OC, Pande GN. Time-dependent multilaminate model of rocks—a numerical study of deformation and failure of rock masses. International Journal for Numerical and Analytical Methods in Geomechanics. 1977 Jul;1(3):219-47.

Pande GN, Sharma KG. Multi-laminate model of clays—a numerical evaluation of the influence of rotation of the principal stress axes. International journal for numerical and analytical methods in geomechanics. 1983 Oct;7(4):397-418.

Bazant ZP, Oh BH. Microplane model for fracture analysis of concrete structures. Northwestern Univ Evanston Il Technological Inst; 1983 May 1.

Amirodin Sadrnejad S. Numerical investigation of hydraulic fracture in saturated cohesive body. InProceedings of the 16th International Conference on Soil Mechanics and Geotechnical Engineering 2005 (pp. 967-970). IOS Press.

SADREJAD S, Pande GN. A multilaminate model for sands. InInternational symposium on numerical models in geomechanics. 3 (NUMOG III) 1989 (pp. 17-27).

Sadrnezhad SA. A Multilaminate Elastic-plastic Model For Liquefaction Of Saturated Sand. InProceeding of the Third International Conference on Seismology and Earthquake Engineering 1999 May 17 (pp. 561-568).

KG, STAGG, and OC ZIENKIEWICZ. "NUMERICAL, ANALYSIS OF DAMS." (1975).

Lee KL, Seed HB, Idriss IM, Makdisi FI. Properties of soil in the San Fernando hydraulic fill dams. Journal of the Geotechnical Engineering division. 1975 Aug;101(8):801-21.

Seed HB, Idriss IM, Lee KL, Makdisi FI. Dynamic analysis of the slide in the Lower San Fernando Dam during the earthquake of February 9, 1971. Journal of the Geotechnical Engineering division. 1975 Sep;101(9):889-911.

Seed HB, Lee KL, Idriss IM, Makdisi FI. The slides in the San Fernando dams during the earthquake of February 9, 1971. Journal of the Geotechnical Engineering Division. 1975 Jul;101(7):651-88.

Ishihara K. Liquefaction and flow failure during earthquakes. Geotechnique. 1993 Sep;43(3):351-451.

Yin ZY, Zhao J, Hicher PY. A micromechanics-based model for sand-silt mixtures. International journal of solids and structures. 2014 Mar 15;51(6):1350-63.